CHEMISTRY OF MATERIALS

pubs.acs.org/cm

Article

Pressure-Induced Superconductivity in the Wide-Band-Gap Semiconductor $Cu_2Br_2Se_6$ with a Robust Framework

Weizhao Cai, Wenwen Lin, Yan Yan, Katerina P. Hilleke, Jared Coles, Jin-Ke Bao, Jingui Xu, Dongzhou Zhang, Duck Young Chung, Mercouri G. Kanatzidis,* Eva Zurek,* and Shanti Deemyad*

Cite This: *Chem. Mater.* 2020, 32, 6237−6246

Read Online

ACCESS | Metrics & More | Article Recommendations | Supporting Information

ABSTRACT: We report pressure-induced superconductivity in a ternary and nonmagnetic Cu-containing semiconductor, $Cu_2Br_2Se_6$, with a wide band gap of 1.89 eV, in which the Cu and Br atoms generate infinite 2_1 helical chains along the *c*-axis and are linked by the cyclohexane-like Se_6 rings to form a three-dimensional framework. We find that this framework is remarkably robust under compression, and the ambient-pressure phase survives at least to our experimental limit of 32.1 GPa. Concurrent semiconductor-to-metal transition and superconductivity are observed above 21.0 GPa. The superconducting temperature monotonically increases from 4.0 to 6.7 K at 40.0 GPa. First-principles calculations show that the emergence of superconductivity is associated with the formation of weak multicentered bonds that involve the increase in coordination of the Cu atoms and a subset of the Se atoms. The observation of superconductivity in this type of nonmagnetic transition-metal-based material will inspire the exploration of related new superconductors under pressure.

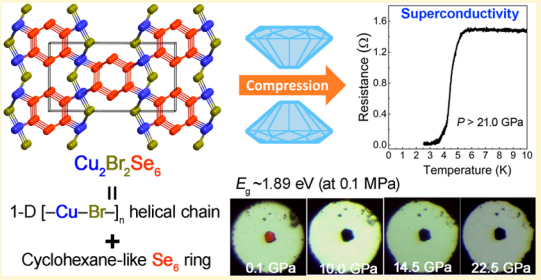

INTRODUCTION

Studies that elucidate how the crystal structure and electronic structure of compounds evolve under pressure are important in the search for new superconductors and in developing a deeper understanding of the mechanisms giving rise to superconductivity. Transition-metal-based compounds, which include both cuprates and Fe-based superconductors, are exceptionally interesting classes of materials.[1−3] Cuprates and Fe-based superconductors have similarities in their structures: whereas cuprates possess two-dimensional (2-D) square CuO_2 planes, Fe-based superconductors are composed of 2-D Fe_2X_2 (X = Se, As) layers that contain edge-sharing FeX_4 tetrahedra.[4,5] The mechanism of superconductivity in both of these classes of unconventional superconductors is still controversial, but it is generally considered to originate from the electron−electron repulsive interaction, which leads to antiferromagnetic fluctuations.[6,7] In both families of superconductors, the transition-metal atoms (Cu and Fe) are magnetically ordered in their parent compounds, and the magnetism is suppressed either by chemical doping or by external pressure before superconductivity appears.[8−11] Moreover, pressure can enhance the superconducting transition temperatures (T_cs).[12−14] These observations have inspired studies of other transition-metal-based chalcogenides under pressure, and a number of unanticipated phenomena, including spin crossover[15,16] and superconductivity,[17,18] have been observed. Similar to the Fe-based superconductors, the transition-metal cations in most other transition-metal-based chalcogenides are magnetically ordered,[18−22] and there are only a few reports of superconductivity in nonmagnetic transition-metal-containing compounds.[23,24]

Previous studies on pressure-induced superconductivity in nonmagnetic metal chalcogenides have mainly been performed on binary semiconductors such as PdS,[25] SnS,[26] GaSe,[27,28] and In_2Se_3.[29] Under compression, these materials usually undergo structural phase transitions, and the coordination of the metal atoms increases progressively. Pressure effectively reduces the interatomic distances, and these structural changes are accompanied by considerable modifications of the electronic structures, e.g., band overlap (metallization), and a transition to the superconducting state.[30] However, only a few studies on pressure-induced superconductivity in metal chalcogenides that do not undergo first-order structural phase transitions have been performed,[31] especially in ternary chalcogenides with a wide energy gap.

The ternary coinage metal halide chalcogenides generally are semiconductors, and at elevated temperature their Ag^+ (Cu^+) ions exhibit high mobility and extraordinary electrical properties; e.g., reversible switching character between p- and n-type

Received: May 22, 2020
Revised: June 20, 2020
Published: June 22, 2020

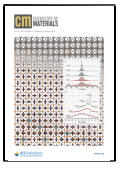

https://dx.doi.org/10.1021/acs.chemmater.0c02151
Chem. Mater. 2020, 32, 6237−6246

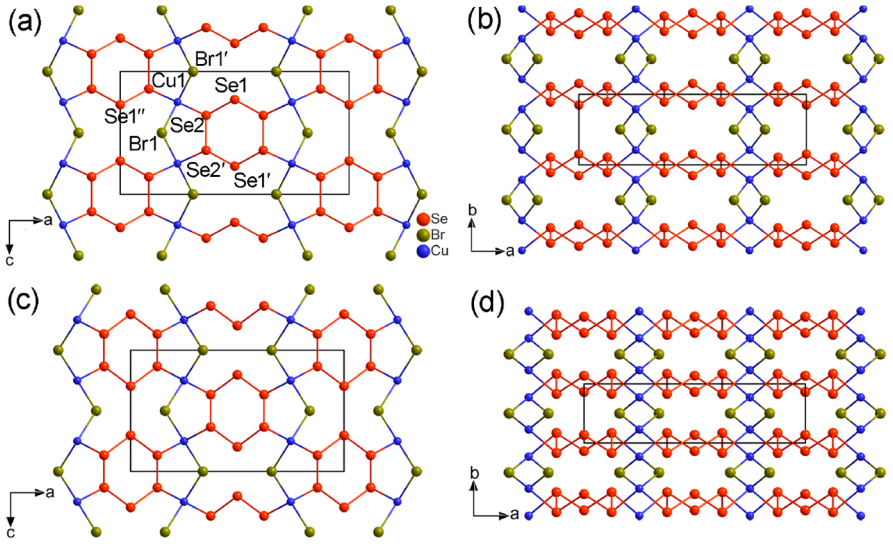

Figure 1. Crystal structures of $Cu_2Br_2Se_6$ viewed along the [010] and [001] directions: (a, b) at 0.3 GPa and (c, d) at 26.4 GPa. Color code: Cu, blue; Br, dark yellow; Se, bright red.

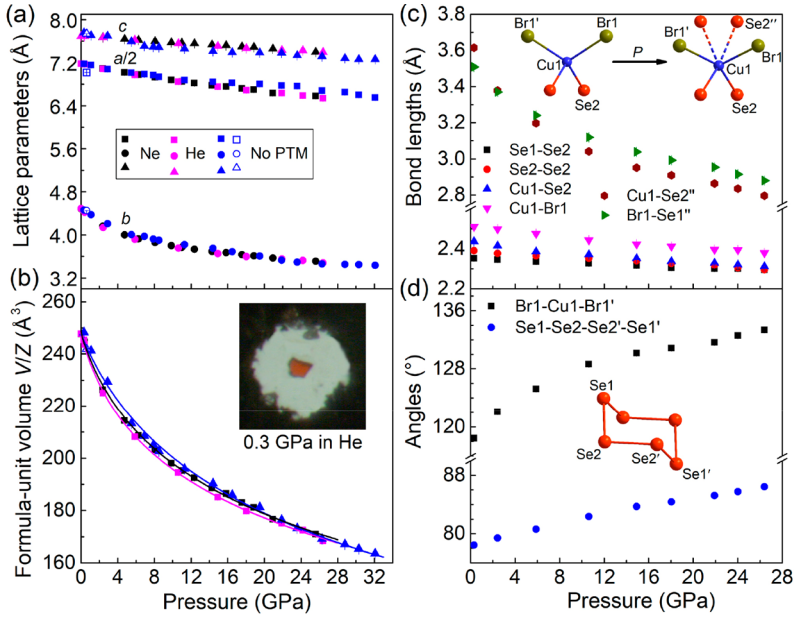

Figure 2. (a) Pressure dependence of the lattice parameters of $Cu_2Br_2Se_6$. The magenta, black, and blue symbols represent crystal data collected in helium, neon and without PTM, respectively. (b) The Birch−Murnaghan equation of state (EOS) fits to the formula-unit volume (V/Z) data. Unfilled symbols represent decompression data. The calculated bulk moduli are given in Table S1. The inset in (b) shows a single crystal in a DAC chamber compressed in helium at 0.3 GPa for X-ray diffraction measurements. (c) Compression of distances between select atom pairs. The way in which the coordination of the Cu1 atoms increases under pressure is shown in the inset. (d) Evolution of the Br1−Cu1−Br1′ angle and the Se1−Se2−Se2′−Se1′ torsion angle under pressure. The inset shows the chair conformation of the Se_6 ring.

conduction is observed by the change of temperature in $Ag_{10}Br_3Te_4$.[32,33] However, high-pressure studies on this family of halide chalcogenides are very rare. Recently, we discovered pressure-induced superconductivity in a wide-band-gap (E_g ~ 1.95 eV) semiconductor, $Cu_2I_2Se_6$, whose structure is composed of cyclohexane-like Se_6 rings and Cu_2I_2 rhomboids in a rhombohedral symmetry.[34] Under pressure two phase transitions occur at ~13.0 and 21.0 GPa, and the latter transition induces superconductivity with a critical temperature of 2.8 K associated with an unanticipated chair-to-planar conformational change of the Se_6 rings in the structure.[35] The emergence of superconductivity by structural modification in this material motivates further studies on analogous copper-containing halide chalcogenides. Here, we report our high-pressure structure and electrical resistivity studies together with first-principles calculations on a compositionally related but structurally different nonmagnetic semiconductor, $Cu_2Br_2Se_6$, whose ambient pressure band gap is 1.89 eV, and its structure is composed of one-dimensional (1-D) $[-Cu-Br-]_n$ helical chains not similar to the Cu_2I_2 rhomboids in $Cu_2I_2Se_6$.

RESULTS AND DISCUSSION

The $Cu_2Br_2Se_6$ single crystals were grown by the vertical three-zone Bridgman method. A mixture of high-purity CuBr and Se

https://dx.doi.org/10.1021/acs.chemmater.0c02151
Chem. Mater. 2020, 32, 6237−6246

powders was heated under vacuum in a temperature gradient of 200−500 °C (see the Experimental Section for details).[36] The phase purity of the resulting $Cu_2Br_2Se_6$ compound was confirmed by powder X-ray diffraction. Differential thermal analysis revealed this material melts congruently at 362 °C with no thermo-induced phase transition (Figure S1). The sample exhibits a sharp optical transition at ∼1.89 eV, consistent with its dark red color (Figure S2). We measured the temperature dependence of the magnetic susceptibility on a crystal sample of $Cu_2Br_2Se_6$ at ambient pressure with a magnetic field of 1 T as shown in Figure S3. The sample shows diamagnetic character above ∼50 K and then a paramagnetic tail down to 1.7 K, which is most likely from the impurities that cannot be detected by powder X-ray diffraction. The diamagnetic behavior indicates that the Cu atom is monovalent (+1).

At ambient pressure the structure of $Cu_2Br_2Se_6$ features an orthorhombic symmetry with space group *Pmna* and $Z = 2$, and it consists of cyclohexane-like Se_6 rings that are interlinked by one-dimensional (1-D) $[-Cu-Br-]_n$ helical chains along the [001] direction (Figure 1). This compound also can be regarded as a composite material with neutral Se_6 rings embedded in an ionic CuBr matrix. Because the absence of one of these sublattices would result in an instability of the whole framework, the structure is a molecular assembly of the neutral Se_6 ring and helical Cu_2Br_2 unit. It is obvious that the structural motifs formed by the Cu and Br atoms are different from those of the Cu and I atoms in $Cu_2I_2Se_6$, in which Cu_2I_2-rhomboids are present.[35] This construction of neutral Se_6 rings within a CuBr matrix indicates that the structure can be understood as $([Cu]^{1+}[Br]^{1-})_2[Se_6]^0$. Assigning Cu to the +1 oxidation state is consistent with the experimentally determined diamagnetic character of this compound.

High-pressure synchrotron single crystal X-ray diffraction (XRD) data of $Cu_2Br_2Se_6$ were collected at room temperature. Helium and neon were used as the pressure transmitting media (PTM). Moreover, polycrystalline X-ray data were also collected without a PTM to investigate the effect of hydrostaticity on the phase stabilities and mimic conditions that resemble electrical resistance measurements. Details of the XRD measurements can be found in the Supporting Information. Unlike $Cu_2I_2Se_6$, the analysis of the X-ray data to the experimental limit of 32.1 GPa reveals no evidence of a structural phase transition, regardless of the different hydrostatic conditions (Figures S4 and S5). As shown in Figure 2a, the lattice parameters contract monotonically with increasing pressure, and the *b*-axis has the largest positive compressibility, whereas the *c*-axis is hard to compress. For example, the *b*-axis is compressed by ∼22.4% in helium up to 26.4 GPa, while the *a*- and *c*-axes are only reduced by 8.9% and 3.8%, respectively. The [010] is the softest direction, which is consistent with the layered-like character of the structure (Figure 1b,d). As shown in Figure 2b, the unit-cell volume data with He as the PTM can be well fitted by the third-order Birch−Murnaghan equation of state, the zero-pressure bulk modulus B_0 is equal to 18.2(8) GPa, and its pressure derivative is $B' = 7.6(4)$. The magnitudes of both B_0 and B' strongly depend on the PTM. For example, when using neon as the PTM, we find $B_0 = 21.8(8)$ GPa and $B' = 6.5(3)$, whereas without a pressure medium $B_0 = 28.7(19)$ GPa, and $B' = 4.7(4)$ (see Table S1). We attribute the observed differences to the presence of non/quasi-hydrostatic conditions.[37]

The 1-D $[-Br-Cu-]_n$ helices extending along the [001] direction undergo drastic distortions under compression; for example, the Br1−Cu1−Br1′ angle increases from 118.42(6)° to 133.3(2)°, and the Cu1−Br1 bond distance shrinks from 2.5102(8) Å at 0.3 GPa to 2.380(2) Å at 26.4 GPa (Figure 2c,d). At low pressure, the Cu1 atom adopts a tetrahedral geometry and is coordinated to two Br1 atoms and two Se2 atoms, and these tetrahedra are further linked to each other via corner-sharing along the *c*-axis. With increasing pressure, the Cu1−Se2″ distance shortens dramatically, i.e., from 3.616(1) Å at 0.3 GPa to 2.796(4) Å at 26.4 GPa. Hence, the coordination of the Cu1 atom increases from 4 to 6 (Figure 2c). Similarly, the Br1−Se1″ distance decreases from 3.5084(9) to 2.879(4) Å at these pressures, with the coordination of Se1 increasing from 2 to 4. Unlike $Cu_2I_2Se_6$, there is only one type of Se_6 ring in $Cu_2Br_2Se_6$. Such a six-membered selenium ring in the chair conformation contains four symmetrically equivalent Se2 atoms and two Se1 atoms. The Se_6 ring is connected to four crystallographically equivalent Cu1 atoms by Cu1−Se2 bonds, whereas the two Se1 atoms do not bond with the Cu1 atoms (Figure 1a). The Cu1−Se2 bond length decreases from 2.437(1) Å at 0.3 GPa to 2.311(3) Å at 26.4 GPa. In contrast to $Cu_2I_2Se_6$, which presents flattening of two-thirds of the Se_6 rings, the neutral Se_6 rings in $Cu_2Br_2Se_6$ do not flatten and only become more distorted without any conformational changes (Figure 2d). Despite this structural stability, the electronic properties of $Cu_2Br_2Se_6$ change dramatically under pressure, and $Cu_2Br_2Se_6$ enters into the metallic and superconducting state above ∼21.0 GPa with $T_c = 4.0$ K. The superconducting temperature increases monotonically and rises to 6.7 K at 40.0 GPa.

Unlike the Se_6 rings in $Cu_2I_2Se_6$, which possess S_3 symmetry, the selenium atoms within the Se_6 rings in $Cu_2Br_2Se_6$ are related to each other by an inversion center and a mirror plane. To track the distortions of the Se_6 rings, we plotted the torsion angle Se1−Se2−Se2′−Se1′ as a function of pressure. As shown in Figure 2c,d, the torsion angle increases monotonically from 78.45(4)° to 86.4(1)° from 0.3 to 26.4 GPa, and the Se1−Se2/Se2−Se2′ bond lengths contract from 2.3520(9)/2.3904(11)Å to 2.294(2)/2.295(3) Å simultaneously. The deformation behavior of the Se_6 rings in $Cu_2Br_2Se_6$ resembles that of the $Cu_2I_2Se_6$ in phase I.[35] As shown in Figure 1a, the conformational changes of the Se_6 rings mainly depend on the evolution of the *y*-coordinates of the Se1 and Se2 atoms under compression. The deformations of the 1-D $[-Br-Cu-]_n$ rigid helices resemble the compression of a mechanical spring, which considerably affects the geometries of the Se_6 rings via the strong covalent Cu1−Se2 interactions. For example, the *y*-coordinate of the Se2 atom decreases gradually from 0.8914(2) at 0.3 GPa to 0.8312(7) at 26.4 GPa. Although the Se1 atom does not covalently bond to the Cu atoms, it cannot move freely under pressure due to the strong internal ring strain. The *y*-coordinate of the Se1 atom decreases abruptly from 0.1522(2) (at 0.3 GPa) to 0.1318(4) (at 5.9 GPa) and then increases gradually up to 0.1375(8) (at 26.4 GPa) (see Figure S6). Hence, the cyclic Se_6 rings become more puckered with increasing pressure, and the chair conformation (cyclohexane-like) is maintained in the whole pressure range.

The $Cu_2Br_2Se_6$ crystal is dark-red and has high resistivity (∼10^{11} Ω·cm) at ambient conditions. Under compression, its dark-red color gradually darkens, and it becomes completely black above ∼9.0 GPa (Figure S7). The prominent piezochromism reveals a gradual closure of the electronic

https://dx.doi.org/10.1021/acs.chemmater.0c02151
Chem. Mater. 2020, 32, 6237−6246

band gap. Figure S8 shows the electrical resistance of a $Cu_2Br_2Se_6$ powder sample measured at room temperature. The resistance reduces continuously with increasing pressure; i.e., the magnitude of resistance drops by almost 7 orders as pressure increases from 2.0 to 20.0 GPa. The reduction rate of the resistance under compression is comparable to that observed in $Cu_2I_2Se_6$[35] and other chalcogenides such as $FePS_3$[15] and SnSe.[38] The temperature-dependent electrical resistance measurements reveal that $Cu_2Br_2Se_6$ displays semiconducting character below ~20.0 GPa (see $R(T)$ curves in Figure 3a and Figure S9). Interestingly, the electrical

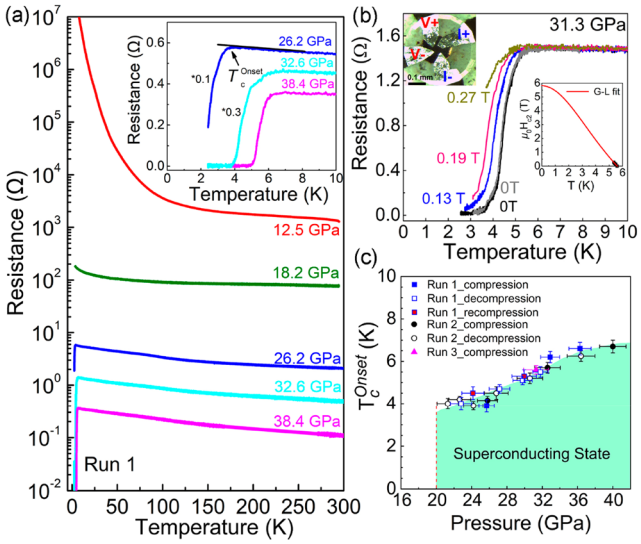

Figure 3. (a) Temperature-dependent electrical resistance at various pressures in $Cu_2Br_2Se_6$. The inset enhances the details of superconducting transitions in the range of 0−10 K. (b) Temperature-dependent resistance at various magnetic fields from 0.0 to 0.27 T at 31.3 GPa. The temperature-dependent resistance was measured before (black) and after (gray) the application of a magnetic field. The left inset indicates the photograph using the four-terminal method for resistivity measurements. The right inset displays the temperature dependence of the upper critical magnetic field. The curve is fitted with the formula of $H_{c2}(T) = H_{c2}(0)(1 - (T/T_c)^2)/(1 + (T/T_c)^2$ based on Ginzburg−Landau (G−L) theory. (c) Pressure dependence of T_c for $Cu_2Br_2Se_6$ from different runs.

resistance increases slightly upon cooling when pressure exceeds 20.0 GPa, indicative of the features of a bad metal (Figure 3a and Figure S9).[39] As clearly shown in Figure 3a, an abrupt decrease of the electrical resistance was observed at about 4.0 K at 26.2 GPa in run 1, indicating the onset of superconductivity. We were unable to observe the resistance drop to zero due to the experimental limitations of the cooling system. At 32.6 GPa, we observed a complete transition and the resistance indeed drops to zero. From a series of compression, decompression, and recompression cycles in both runs 1 and 2, we confirmed the superconducting state of $Cu_2Br_2Se_6$ exists above 21.0 GPa. Further decompression to 20.0 GPa leads to the re-emergence of semiconducting properties (Figure S9d). We find T_c gradually increases with increasing pressure and reaches 6.7 K at 40.0 GPa, and a dope-shaped $T_c(P)$ is anticipated if the sample were compressed to higher pressures (Figure 3c).

Even though the presence of impurities suggests that a percolated superconducting path may occur, the impurity level is very small (<0.1%), as confirmed by synchrotron X-ray diffraction, thereby ruling out this possibility. In all cases the drop in resistivity at the superconducting transition was nearly complete, and at several pressure points we not only observed the onset of the superconducting transition but also measured zero resistance (Figure 3). This requires the superconducting portion of the sample to exceed the percolation threshold, which is about 16% for a random 3D lattice and larger for ordered structures.[40−43] If the superconductivity were a result of the minute amount of impurities, zero resistance could not be achieved since the impurity level is significantly below the percolation limit. To confirm the emergence of bulk superconductivity in the $Cu_2Br_2Se_6$ sample, we measured the change in T_c upon the application of an external magnetic field at 31.3 GPa (Figure 3b). As the magnetic field increases to 0.27 T, T_c is seen to shift progressively to lower temperatures. From the fit $H_{c2}(T) = H_{c2}(0)(1 - (T/T_c)^2)/(1 + (T/T_c)^2$ based on Ginzburg−Landau (G−L) theory, the upper critical field at 31.3 GPa is estimated to be 5.8 T (right inset in Figure 3b). The magnitude of the estimated critical field is about 1.8 times lower than the Bardeen, Cooper, and Schrieffer (BCS) weak-coupling Pauli limiting field $\mu_0 H_p(0) = 1.84 T_c = 10.3$ T.[44]

Density functional theory calculations were performed to gain further insight into the relationship between the structural distortions that occur within *Pmna*-$Cu_2Br_2Se_6$ under pressure and the resulting changes in the electronic structure and emerging superconductivity. As shown in Table S3, the lattice constants calculated with the PBE functional were within 2.5% of those obtained experimentally, with the exception of the *b* lattice parameter at 0.3 GPa, which was somewhat overestimated. The reason for the discrepancy is that the dispersion interactions between the layers within which the Se_6 rings lie are not captured by the PBE functional (as verified by a functional that accounts for dispersion semiempirically, see Table S3). However, as pressure increases, the van der Waals interactions become less important, yielding excellent agreement between the theoretical and experimental lattice parameters calculated by PBE. Phonon calculations confirm the dynamic stability of the *Pmna* phase up to 23.0 GPa (Figure S10).

To better understand the evolution of the bonding under pressure, we calculated the negative of the crystal orbital Hamilton populations integrated to the Fermi level (-ICOHP)[45] for various atom pairs, as shown in Table 1. Pressure strengthens the Cu1−Br1 and Se2−Se2′ bonds, whose distance decreases, as expected. However, the -ICOHP between Cu1−Se2 decreases slightly at elevated pressure even though the bond between these two atoms shortens. This Cu1−Se2 bond lies *trans* to a Cu1−Se2″ contact which measures 4.039 Å at 0.3 GPa (within PBE) but is shortened significantly to 2.723 Å by 21.9 GPa as a result of the large decrease of the *b* lattice parameter. Therefore, as Cu1 begins to interact with Se2″, the strength of the original Cu1−Se2 interaction decreases, and the coordination environment around the Cu1 changes from tetrahedral to quasi-octahedral, as shown in the inset of Figure 2c. Whereas in a perfect octahedron the Br1−Cu1−Br1′ angle would be 180°, our computations yield 138°, a distortion resulting from the Br1 lone pairs (as shown in the plots of the electron localization function, Figure S13). Similarly, the Se1−Se2 bond weakens slightly under pressure as each Se1 begins to interact with two Br1 atoms that are 2.897 Å away, thereby approaching square-planar-like coordination. At 21.9 GPa the calculated -ICOHPs

https://dx.doi.org/10.1021/acs.chemmater.0c02151
Chem. Mater. 2020, 32, 6237−6246

Table 1. Select Distances in *Pmna*-$Cu_2Br_2Se_6$ at 0.3 and 21.9 GPa and Their Corresponding Crystal Orbital Hamilton Populations Integrated to the Fermi Level (-ICOHPs) Calculated by Using the PBE Functional

	P = 0.3 GPa[a]		P = 21.9 GPa	
bond	distance (Å)	-ICOHP (eV/bond)	distance (Å)	-ICOHP (eV/bond)
Cu1−Br1	2.524	1.15	2.423	1.21
Cu1−Se2	2.382	1.56	2.360	1.41
Cu1−Se2″	4.039	0.03	2.723	0.60
Cu1−Se1	3.627	0.06	3.315	0.05
Se1−Se2	2.385	4.08	2.342	3.91
Se2−Se2′	2.465	3.24	2.386	3.41
Se2−Br1 (along *a*)	3.488	0.12	3.200	0.17
Se2−Br1 (along *c*)	3.597	0.09	3.030	0.28
Se1−Br1″	3.630	0.08	2.897	0.47

[a]At 0.3 GPa all of the -ICOHPs, with the exception of the one computed for Se2−Se2′, are within 0.05 eV/bond of the results obtained with PBE-D3 (see Table S5).

are 1.41, 1.21, 0.60, and 0.47 eV/bond for Cu1−Se2 (short), Cu1−Br1, Cu1−Se2″ (long), and Se1−Br1″, respectively. Even though the multicenter bonding interactions that are expected to emerge under pressure are weak,[30] they coincide with important changes in the electronic structure and properties of this phase. To investigate whether the increase of the coordination numbers of the Cu1 and Br1 atoms results in a change of their oxidation states under pressure, a Bader charge analysis was performed. The results (Table S4) show the charges on the Cu1 atom at 0.3 and 21.9 GPa are comparable (0.43*e* vs 0.41*e*), revealing that the monovalent nature of the Cu1 atom is maintained at high pressure, whereas the charge on the Br1 atom becomes slightly less negative with increasing pressure (−0.53*e* vs −0.41*e*).

The electronic band structures and projected density of states of *Pmna*-$Cu_2Br_2Se_6$ were calculated at 0.3, 10.6, and 21.9 GPa (Figure 4a, Figures S11 and S12). The PBE calculations, which are expected to underestimate the band gap, find that this phase is a semiconductor with an indirect band gap of 0.92 eV at 0.3 GPa, with the top of the valence band at the Y-point and the bottom of the conduction band at the U-point. By 10.6 GPa the band gap becomes direct, and it is located at the Y-point. Such an indirect (Y−U) to direct (Y−Y) pressure-induced transition in the band gaps was previously calculated to occur within $Cu_2I_2Se_6$ by 12.5 GPa.[35] At 21.9 GPa, $Cu_2Br_2Se_6$ is found to be a weak metal, and the insulator-to-metal transition is a result of pressure-induced band broadening that arises due to increased orbital overlap. Moreover, the metallization occurs via donation of Cu(I) d states to unoccupied p−p σ-antibonding functions within the Se_6 rings, in an example of metal-to-ligand charge transfer, which is accompanied by an increase in Cu coordination by Se under pressure. It could be expected that further Cu → Se charge transfer would yield $Cu(II)Br^-$ along with Se_6^- ligands at higher pressures, provided this phase is stable.

The calculated results are well consistent with electrical resistance measurements as discussed above. At 21.9 GPa, the three bands that cross the Fermi level, E_F, are primarily of Cu1-d, Br1-p, and Se1/Se2-p character (Figure S12c). One of them is a doubly degenerate occupied band that rises above E_F along the U−R high-symmetry line, and two empty bands dip below

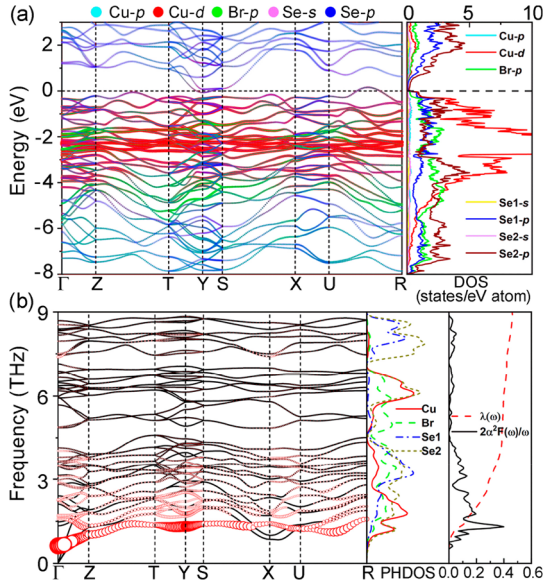

Figure 4. (a) Electronic band structure projected onto atomic orbitals that are represented by colored circles whose radius is proportional to their contribution (fat bands). The projected density of states (DOS) is shown in the right panel. (b) Phonon band structure (the radius of the red circles is proportional to the phonon line width) and projected phonon density of states (PHDOS). The right panel shows the Eliashberg spectral function, in the form of $2\alpha^2F(\omega)/\omega$, and the integrated electron phonon coupling parameter, $\lambda(\omega)$.

E_F along the T−Y−S high-symmetry lines. The latter set of bands are nearly parallel to each along the T−Y high-symmetry line, yielding a Fermi surface that is nested.

The features in the density of states at 21.9 GPa in $Cu_2Br_2Se_6$ differ from what was calculated for $Cu_2I_2Se_6$ (at 22.0 GPa), where the Se-p states contributed predominantly to the total density of states around the Fermi level because of the flattened Se_6 rings (see Figure S14).[35] The structural peculiarities of these two compounds also result in a large difference in the magnitude of their calculated density of states at the Fermi level, i.e., 3.89 state/eV/fu for $Cu_2I_2Se_6$ (at 22.0 GPa) and 0.40 states/eV/fu for $Cu_2Br_2Se_6$ (at 21.9 GPa). Because I is heavier than Br, the Debye frequencies of these phases differ. Therefore, despite the closeness of the observed T_cs in both materials (∼4.0 K), the lattice and electronic contributions that give rise toward the superconducting state in them differ.

The phonon band structure of $Cu_2Br_2Se_6$ at 21.9 GPa can be divided into three regions that are separated by gaps (Figure 4b). The lower frequency (0−4.7 THz) modes are associated with motions of all of the atoms, the intermediate region (4.7−7.2 THz) is from the Cu1, Br1, and Se2 atoms, and the higher frequency modes arise from the Se1 and Se2 atoms. The electron−phonon coupling (EPC) resulting from vibrations in these regions contributes 83.9, 7.5, and 8.6% toward the total EPC parameter, λ. The first optical phonon mode possesses a large line width throughout most of the Brillouin zone (the line width is somewhat smaller around the X and R points). Although contributions from all atom types are found in the projected phonon densities of states in this frequency range (0.63−1.58 THz), those from Cu1 and Se2 are predominant. Visualization of the first optical mode at the Γ-point shows that the Cu1 atoms move perpendicular to the axis of the $[-Cu-Br-]_n$ helical chains, and at the same time the four Se2 atoms

https://dx.doi.org/10.1021/acs.chemmater.0c02151
Chem. Mater. 2020, 32, 6237−6246

coordinated to a single Cu1 move in a rocking motion about it. Over the course of the vibration, the Cu1 atom maintains two short Cu1−Se2 distances of around 2.35−2.37 Å and two longer ones of about 2.66−2.79 Å. The bonds whose lengths change the most during the vibration are the Cu1−Se2″, Cu1−Br1, and Se2−Se2′. At the Y-point the Cu1 atoms undergo the largest displacement. They move along the *b*-axis as if forming dimers, with the Cu1−Cu1′ distances changing from 3.17 to 3.91 Å during the course of the vibration. As a result, every other Cu1 achieves a nearly square-planar coordination by the surrounding Se2 atoms (Cu1−Se2 distances of 2.45−2.68 Å and Se2−Cu1−Se2″ angles of 87°−92°), with the other Cu1 coordination being much more distorted (2.15−2.89 Å and 80°−109°). The Se2−Se2′, Se1−Se2, and Br1−Cu1 bond lengths are also modified during the course of the vibration, but to a lesser extent. The mode at the Z-point is perhaps the most complex. In it the motions of the Cu1 and Se2 atoms primarily affect the Cu1−Br1, Se1−Br1, and Se1−Se2 distances. From visualizing these three modes, which are only a subset of those that have a substantial line width, we can conclude that changes in both the strong (Se2−Se2′, Se1−Se2, Cu1−Se2, and Cu1−Br1), and the weak (Cu1−Se2″ and Se1−Br1″) bonds are important for the superconducting mechanism.

Our calculations yield a moderate EPC parameter, λ, of 0.46 and a relatively low logarithmic average of phonon frequencies, ω_{log}, of 117.7 K. These values were employed within the Allen−Dynes modified McMillan formula[46] by using a typical value of the Coulomb pseudopotential, $\mu^* = 0.1$ and 0.13, to estimate the superconducting critical temperature, T_c, as 1.0 and 0.6 K, respectively, at 21.9 GPa. The low T_c stems from the fact that *Pmna*-$Cu_2Br_2Se_6$ has a small density of states at E_F and because it is composed of heavy atoms that do not have high-frequency phonon modes. Thus, this phase is a conventional superconductor, and the electron−phonon coupling mechanism involves contributions from weak multicentered bonds that are formed under pressure. The pressure dependence of T_c in conventional superconductors is a complex problem that depends on both the electronic and lattice properties. While, for example, in simple metal superconductors a shift of the phonon spectrum to higher frequencies leads to weakening of the electron−phonon coupling and causes negative $dT_c(P)/dP$ dependence, in the case of some transition metal superconductors, the electronic enhancement dominates. In the present case of $Cu_2Br_2Se_6$, we find an almost purely electronic effect in the absence of structural instabilities in a remarkably large range of pressures.

CONCLUSIONS

In conclusion, we find that pressure-induced band-gap closure occurs in the wide-band-gap semiconductor $Cu_2Br_2Se_6$ without any structural phase transition. Electrical transport measurements and first-principles calculations reveal a semiconductor-to-metal transition and superconductivity in $Cu_2Br_2Se_6$ at about 21.0 GPa. In contrast to what is observed in the analogous $Cu_2I_2Se_6$ compound, the different framework of $Cu_2Br_2Se_6$ is extremely robust in response to high external pressure. First-principles calculations suggest that the large distortions of the 1-D $[-Br-Cu-]_n$ helices under compression promote the formation of multicenter bonds and affect the electronic structure substantially, and these distinct bond modifications are at least in part responsible for the occurrence of conventional superconductivity. The emergence of conventional superconductivity under pressure due to purely electronic enhancement in this copper-based halide chalcogenide opens the route to seek related classes of new superconductors by using pressure as an approach.

EXPERIMENTAL METHODS

Synthesis and Crystal Growth of $Cu_2Br_2Se_6$. *Caution! Selenium and its compounds are toxic, and great precautions should be taken.* 14.345 g of CuBr (Sigma-Aldrich, 99.999% purity) was mixed with 23.688 g of selenium (Sigma-Aldrich, 99.999% purity) and then loaded into a silica ampule (inner diameter: 10 mm; outer diameter: 13 mm) with a conical tip, and then the ampule was flame-sealed under a residual pressure of 10^{-4} Pa. The mixture was heated over 6 h, melted at 500 °C for 24 h, and then cooled to room temperature over 24 h.

The crystal growth was conducted in a vertical three-zone Bridgman furnace with a growth speed of 0.5 mm/h and a temperature gradient of 9.5 °C/cm. The ampule was kept still at the top hot zone for 24 h to ensure complete melting before crystal growth. The temperatures for the hot zone, the middle zone, and the bottom zone of the Bridgman furnace were set at 550, 450, and 200 °C, respectively. After completion of the crystal growth, the ampule was kept in the bottom zone at 200 °C for postannealing to reduce thermal stress for 2 days. After annealing, the ampule was dropped down at a translation speed of 5 mm/h until it reached room temperature.

Optical Properties Measurements. Solid-state diffusion reflectance was performed on a ground powder sample of $Cu_2Br_2Se_6$ by using a Shimadzu UV-3600PC double-beam, double-monochromator spectrophotometer operating in the 200−2500 nm region.

Thermal Analysis. Differential thermal analysis (DTA) was performed on a powder sample of $Cu_2Br_2Se_6$ to check its thermal stability by using a Netzsch STA 449F3 Jupiter thermal analyzer. Grounded polycrystalline material (∼55 mg) was flame-sealed in a silica ampule and evacuated to 10^{-4} mbar. As a reference, a similarly sealed ampule of ∼30 mg of Al_2O_3 was used. The sample was heated to 580 °C at 5 °C min^{-1} and then cooled at 5 °C min^{-1} to 20 °C.

Magnetic Measurements. Magnetic susceptibility measurements in the temperature range of 1.8−300 K at ambient pressure were performed on a $Cu_2Br_2Se_6$ polycrystalline piece with a mass of 35.7 mg in a Magnetic Property Measurement System (Quantum Design, MPMS 3 SQUID magnetometer). The sample was fixed by a negligible amount of GE varnish on a quartz sample holder, and the applied magnetic field was $\mu_0 H = 1$ T.

High-Pressure X-ray Diffraction Measurements. The Boehler-Almax plate diamond anvil cells (DACs) with 500 μm culet size and an opening angle of about 60° were used for all high-pressure single-crystal X-ray measurements. The pressure was calibrated by the ruby fluorescence method and was measured before and after each diffraction data collection.[47]

To investigate the effect of hydrostaticity on the phase stabilities of $Cu_2Br_2Se_6$, helium (He) and neon (Ne) were used as pressure-transmitting media.[37] Plate-shaped single crystals of $Cu_2Br_2Se_6$ with dimensions 35 × 25 × 10 μm^3 for He and 40 × 24 × 12 μm^3 for Ne were loaded in initial ∼220 μm diameter and ∼65 μm thickness rhenium or stainless steel gasket chambers. The high-pressure single-crystal X-ray data were collected up to 25.6 GPa in Ne and 26.4 GPa for He at room temperature.

All high-pressure single-crystal X-ray diffraction data of $Cu_2Br_2Se_6$ were collected at beamline 13-BM-C, GSECARS of the Advanced Photon Source (APS), Argonne National Laboratory (ANL). The X-ray wavelength was 0.4341 Å. Diffraction data were collected by using a PILATUS3 1M (Dectris) detector. The exposure time was set as 1 s/deg, and each diffraction image covered 1 deg in the φ-axis. The collected X-ray images were reduced by using the APEX3 package.[48] The crystal structures of $Cu_2Br_2Se_6$ can be solved by the direct method using SHELXS-97[49] and refined with SHELXL interfaced by Olex2-1.2.[50] All the Cu, Br, and Se atoms were refined anisotropically.

https://dx.doi.org/10.1021/acs.chemmater.0c02151
Chem. Mater. 2020, 32, 6237−6246

To mimic conditions similar to the electric resistance measurements, the polycrystalline sample of $Cu_2Br_2Se_6$ was loaded into an ~150 μm hole of an ~65 μm thick stainless steel gasket without pressure medium and pressurized in a Boehler-Almax plate DAC. The pressure was determined by the ruby fluorescence method.[47] The diffraction data were collected up to 32.1 GPa at room temperature at the 16-ID-B beamline of the High Pressure Collaborative Access Team (HPCAT) at APS, ANL (λ = 0.4066 Å). The image data were integrated by using the Dioptas program.[51] The X-ray diffraction data were analyzed by the Le Bail fitting method using the GSAS-EXPGUI package.[52] The single crystal structure data were used as the starting models to carry out all the refinements.

High-Pressure Electrical Transport Measurements. High-pressure electrical resistance measurements of $Cu_2Br_2Se_6$ were conducted by four- and quasi-four-terminal method. Fine alumina powder mixed with epoxy was used as an insulating layer. Diamond anvils with 500 and 350 μm culet size were used for the measurements. Stainless steel and nonmagnetic Re gaskets with ~250 and 130 μm holes were employed in different runs. Platinum electrodes were cut from a 5 μm thick foil and were arranged to measure the resistivity of the sample by the four-terminal technique. An ac technique was used at 17.77 Hz frequency from a Stanford Research SR830 digital lock-in amplifier for all the measurements. A closed cycle He cryostat was employed to examine the temperature dependence of the electrical resistance at specific pressures in the range of 2.4−300 K. Electrical resistance data at various magnetic fields were collected in a homemade copper coil by using a nonmagnetic copper beryllium (CuBe) DAC. The pressure was determined using the ruby fluorescence method at both RT and a low temperature of ~4.0 K with the aid of an online ruby system.

Computational Details. Geometry optimizations and electronic structure calculations including density of states (DOS), band structures, electron localization functions (ELFs),[53] and Bader charges of $Cu_2Br_2Se_6$ in the *Pmna* space group were performed in the framework of density functional theory (DFT) as implemented in the Vienna *Ab Initio* Simulation Package (VASP)[54,55] with the gradient corrected exchange and correlation functional of Perdew−Burke−Ernzerhof (PBE-GGA).[56] The projector augmented wave (PAW) method[57] was used to treat the core states, and a plane-wave basis set with an energy cutoff of 400 eV was employed for precise optimizations. The structure was also optimized at 0.3 GPa by using the DFT-D3 functional[58] to determine whether van der Waals interactions are important for the structural parameters at low pressures. The Se $4s^24p^4$, Br $4s^24p^5$, and Cu $3d^{10}4s^1$ electrons were treated explicitly in all calculations. The *k*-point grids were generated using the Γ-centered Monkhorst−Pack scheme,[59] and the number of divisions along each reciprocal lattice vector was chosen such that the product of this number with the real lattice constant was 70 Å. The bonding of select phases was further analyzed by calculating the crystal orbital Hamilton populations (COHP) and the negative value of the COHP integrated to the Fermi level (-ICOHP) by using the LOBSTER package.[45,60,61]

Phonon band structures were calculated by using the supercell approach. Hellmann−Feynman forces were calculated from a supercell constructed by replicating the optimized structure wherein the atoms had been displaced, and dynamical matrices were computed by using the PHONOPY code.[62] The Quantum Espresso (QE)[63] program was used to obtain the dynamical matrix and electron−phonon coupling (EPC) parameters. Calculations were performed using the PBE-GGA,[56] pseudopotentials that were obtained from the QE pseudopotential library, and an energy cutoff of 120 Ry. The pseudopotentials were generated by the Troullier−Martins method[64] with valence configurations of $4s^24p^4$ for Se, $4s^24p^5$ for Br, and $3d^94s^2$ for Cu. The superconducting calculations employed a 2 × 6 × 3 *q*-point grid and a 4 × 12 × 6 *k*-point mesh. The Gaussian broadening employed to obtain the EPC parameter, λ, was 0.045 Ry to approximate the zero-width limit in the calculation of λ.

The superconducting transition temperature, T_c, can be estimated using the Allen−Dynes modified McMillan equation as[46]

$$T_c = \frac{\omega_{log}}{1.2} \exp\left[-\frac{1.04(1+\lambda)}{\lambda - \mu^*(1+0.62\lambda)}\right] \quad (1)$$

where ω_{log} is the logarithmic average frequency, λ is the electron−phonon coupling parameter, and μ^* is the Coulomb pseudopotential, often assumed to be between 0.1 and 0.13. The line width, γ_{qj}, of a phonon mode *j* at a wave vector *q* which results from the electron−phonon coupling is given by

$$\gamma_{qj} = 2\pi\omega_{qj} \sum_{knm} |g^j_{kn,k+qm}|^2 \delta(\epsilon_{kn} - \epsilon_F)\delta(\epsilon_{k+qm} - \epsilon_F) \quad (2)$$

where ϵ_F is the Fermi energy, the sum is over the Brillouin zone, and $g^j_{kn,k+qm}$ is the electron−phonon matrix element.

From the line widths one may obtain the Eliashberg spectral function, $\alpha^2F(\omega)$, as

$$\alpha^2F(\omega) = \frac{1}{2\pi g(\epsilon_F)} \sum_{qj} \frac{\gamma_{qj}}{\omega_{qj}} \delta(\hbar\omega - \hbar\omega_{qj}) \quad (3)$$

where $g(\epsilon_F)$ is the electronic density of states at the Fermi level. The electron−phonon coupling parameter and the logarithmic average frequency are calculated from the Eliashberg spectral function via

$$\lambda = 2\int_0^\infty \frac{\alpha^2F(\omega)}{\omega} d\omega \quad (4)$$

and

$$\omega_{log} = \exp\left[\frac{2}{\lambda}\int \frac{d\omega}{\omega}\alpha^2F(\omega)\log\omega\right] \quad (5)$$

■ ASSOCIATED CONTENT

Supporting Information

The Supporting Information is available free of charge at https://pubs.acs.org/doi/10.1021/acs.chemmater.0c02151.

Ambient-pressure differential thermal analyses, optical absorption spectrum, magnetic susceptibility, high-pressure synchrotron X-ray powder diffraction data, changes of structural parameters under pressure, high-pressure electrical transport data, selective crystallographic single crystal data, phonon and electronic band structures, projected densities of states, electron localization functions, lattice parameters, Bader charges and -ICOHPs calculated for $Cu_2Br_2Se_6$ at various pressures (PDF)

■ AUTHOR INFORMATION

Corresponding Authors

Mercouri G. Kanatzidis − *Materials Science Division, Argonne National Laboratory, Lemont, Illinois 60439, United States; Department of Chemistry, Northwestern University, Evanston, Illinois 60208, United States;* orcid.org/0000-0003-2037-4168; Email: m-kanatzidis@northwestern.edu

Eva Zurek − *Department of Chemistry, State University of New York at Buffalo, Buffalo, New York 14260-3000, United States;* orcid.org/0000-0003-0738-867X; Email: ezurek@buffalo.edu

Shanti Deemyad − *Department of Physics and Astronomy, University of Utah, Salt Lake City, Utah 84112, United States;* orcid.org/0000-0001-5661-8801; Email: Deemyad@physics.utah.edu

Authors

Weizhao Cai − *Department of Physics and Astronomy, University of Utah, Salt Lake City, Utah 84112, United States;* orcid.org/0000-0001-7805-2108

https://dx.doi.org/10.1021/acs.chemmater.0c02151
Chem. Mater. 2020, 32, 6237−6246

Wenwen Lin − *Materials Science Division, Argonne National Laboratory, Lemont, Illinois 60439, United States*
Yan Yan − *Department of Chemistry, State University of New York at Buffalo, Buffalo, New York 14260-3000, United States*
Katerina P. Hilleke − *Department of Chemistry, State University of New York at Buffalo, Buffalo, New York 14260-3000, United States*
Jared Coles − *Department of Physics and Astronomy, University of Utah, Salt Lake City, Utah 84112, United States*
Jin-Ke Bao − *Materials Science Division, Argonne National Laboratory, Lemont, Illinois 60439, United States;* orcid.org/0000-0001-5522-3605
Jingui Xu − *PX2, Hawaii Institute of Geophysics and Planetology, University of Hawaii at Manoa, Honolulu, Hawaii 96822, United States*
Dongzhou Zhang − *PX2, Hawaii Institute of Geophysics and Planetology, University of Hawaii at Manoa, Honolulu, Hawaii 96822, United States*
Duck Young Chung − *Materials Science Division, Argonne National Laboratory, Lemont, Illinois 60439, United States*

Complete contact information is available at: https://pubs.acs.org/10.1021/acs.chemmater.0c02151

Author Contributions

W.L. and Y.Y. contributed equally to this work.

Notes

The authors declare no competing financial interest.

■ ACKNOWLEDGMENTS

We acknowledge Dr. Sergy Tkachev for assistance with helium loading and Dr. Jesse Smith for experimental support and Tushar Bhowmick, Mahé Lezoualc'h, Jordan Lybarger, and Elizabeth Mulvey for their help with high-pressure X-ray data collection. The high-pressure single crystal X-ray diffraction data and powder X-ray diffraction data were collected at 13-BM-C of GeoSoilEnviroCARS (The University of Chicago, Sector 13) and at 16-ID-B of HPCAT (Sector 16), Advanced Photon Source (APS), Argonne National Laboratory, respectively. GeoSoilEnviroCARS was supported by the National Science Foundation-Earth Sciences (EAR-1634415) and Department of Energy-GeoSciences (DE-FG02-94ER14466). HPCAT operations were supported by DOE-NNSA's Office of Experimental Sciences. Use of the COMPRES-GSECARS gas loading system and PX2 was supported by COMPRES under NSF Cooperative Agreement EAR-1661511 and by GSECARS through NSF grant EAR-1634415 and DOE grant DE-FG02-94ER14466. Work at Argonne (sample preparation, characterization, and crystal growth) was supported by the U.S. Department of Energy, Office of Science, Basic Energy Sciences, Materials Science and Engineering Division. Use of the Advanced Photon Source at Argonne National Laboratory was supported by the U.S. Department of Energy, Office of Science, Office of Basic Energy Sciences, under Contract DE-AC02-06CH11357. This material is based upon work supported by the U.S. Department of Energy, Office of Science, Fusion Energy Sciences under Award DE-SC0020340 (E.Z., Y.Y., and S.D.). K.H. is thankful to the U.S. Department of Energy, National Nuclear Security Administration, through the Capital-DOE Alliance Center under Cooperative Agreement DE-NA0003858 for financial support. E.Z., Y.Y., and K.H. acknowledge computational support from the Center for Computational Research (CCR) at SUNY Buffalo. J.C. acknowledges research travel funds from University of Utah Office of Undergraduate Research.

■ REFERENCES

(1) Bednorz, J. G.; Müller, K. A. Possible high Tc superconductivity in the Ba−La−Cu−O system. *Z. Phys. B: Condens. Matter* **1986**, *64*, 189−193.
(2) Kamihara, Y.; Watanabe, T.; Hirano, M.; Hosono, H. Iron-Based Layered Superconductor $La[O_{1-x}F_x]FeAs$ (x = 0.05−0.12) with T_c = 26 K. *J. Am. Chem. Soc.* **2008**, *130*, 3296−3297.
(3) Fang, M.-H.; Wang, H.-D.; Dong, C.-H.; Li, Z.-J.; Feng, C.-M.; Chen, J.; Yuan, H. Q. Fe-based superconductivity with T_c = 31 K bordering an antiferromagnetic insulator in (Tl,K) Fe_xSe_2. *Europhys. Lett.* **2011**, *94*, 27009.
(4) Paglione, J.; Greene, R. L. High-temperature superconductivity in iron-based materials. *Nat. Phys.* **2010**, *6*, 645.
(5) Bednorz, J. G.; Muller, K. A. Perovskite-type oxides—The new approach to high-T_c superconductivity. *Rev. Mod. Phys.* **1988**, *60*, 585−600.
(6) Chen, X.; Dai, P.; Feng, D.; Xiang, T.; Zhang, F.-C. Iron-based high transition temperature superconductors. *Natl. Sci. Rev.* **2014**, *1*, 371−395.
(7) Scalapino, D. J. A common thread: The pairing interaction for unconventional superconductors. *Rev. Mod. Phys.* **2012**, *84*, 1383−1417.
(8) Cava, R. J.; Batlogg, B.; Krajewski, J. J.; Rupp, L. W.; Schneemeyer, L. F.; Siegrist, T.; vanDover, R. B.; Marsh, P.; Peck, W. F., Jr.; Gallagher, P. K.; Glarum, S. H.; Marshall, J. H.; Farrow, R. C.; Waszczak, J. V.; Hull, R.; Trevor, P. Superconductivity near 70 K in a new family of layered copper oxides. *Nature* **1988**, *336*, 211.
(9) Schilling, A.; Cantoni, M.; Guo, J. D.; Ott, H. R. Superconductivity above 130 K in the Hg−Ba−Ca−Cu−O system. *Nature* **1993**, *363*, 56.
(10) Rotter, M.; Pangerl, M.; Tegel, M.; Johrendt, D. Superconductivity and Crystal Structures of $(Ba_{1-x}K_x)Fe_2As_2$ (x = 0−1). *Angew. Chem., Int. Ed.* **2008**, *47*, 7949−7952.
(11) Gao, P.; Sun, L.; Ni, N.; Guo, J.; Wu, Q.; Zhang, C.; Gu, D.; Yang, K.; Li, A.; Jiang, S.; Cava, R. J.; Zhao, Z. Pressure-Induced Superconductivity and Its Scaling with Doping-Induced Superconductivity in the Iron Pnictide with Skutterudite Intermediary Layers. *Adv. Mater.* **2014**, *26*, 2346−2351.
(12) Mizuguchi, Y.; Tomioka, F.; Tsuda, S.; Yamaguchi, T.; Takano, Y. Superconductivity at 27K in tetragonal FeSe under high pressure. *Appl. Phys. Lett.* **2008**, *93*, 152505.
(13) Takahashi, H.; Sugimoto, A.; Nambu, Y.; Yamauchi, T.; Hirata, Y.; Kawakami, T.; Avdeev, M.; Matsubayashi, K.; Du, F.; Kawashima, C.; Soeda, H.; Nakano, S.; Uwatoko, Y.; Ueda, Y.; Sato, T. J.; Ohgushi, K. Pressure-induced superconductivity in the iron-based ladder material $BaFe_2S_3$. *Nat. Mater.* **2015**, *14*, 1008.
(14) Sun, L.; Chen, X.-J.; Guo, J.; Gao, P.; Huang, Q.-Z.; Wang, H.; Fang, M.; Chen, X.; Chen, G.; Wu, Q.; Zhang, C.; Gu, D.; Dong, X.; Wang, L.; Yang, K.; Li, A.; Dai, X.; Mao, H.-k.; Zhao, Z. Re-emerging superconductivity at 48 K in iron chalcogenides. *Nature* **2012**, *483*, 67.
(15) Wang, Y.; Ying, J.; Zhou, Z.; Sun, J.; Wen, T.; Zhou, Y.; Li, N.; Zhang, Q.; Han, F.; Xiao, Y.; Chow, P.; Yang, W.; Struzhkin, V. V.; Zhao, Y.; Mao, H.-k. Emergent superconductivity in an iron-based honeycomb lattice initiated by pressure-driven spin-crossover. *Nat. Commun.* **2018**, *9*, 1914.
(16) Wang, Y.; Zhou, Z.; Wen, T.; Zhou, Y.; Li, N.; Han, F.; Xiao, Y.; Chow, P.; Sun, J.; Pravica, M.; Cornelius, A. L.; Yang, W.; Zhao, Y. Pressure-Driven Cooperative Spin-Crossover, Large-Volume Collapse, and Semiconductor-to-Metal Transition in Manganese(II) Honeycomb Lattices. *J. Am. Chem. Soc.* **2016**, *138*, 15751−15757.
(17) Chi, Z.-H.; Zhao, X.-M.; Zhang, H.; Goncharov, A. F.; Lobanov, S. S.; Kagayama, T.; Sakata, M.; Chen, X.-J. Pressure-Induced Metallization of Molybdenum Disulfide. *Phys. Rev. Lett.* **2014**, *113*, 036802.

(18) Pocha, R.; Johrendt, D.; Ni, B.; Abd-Elmeguid, M. M. Crystal Structures, Electronic Properties, and Pressure-Induced Superconductivity of the Tetrahedral Cluster Compounds $GaNb_4S_8$, $GaNb_4Se_8$, and $GaTa_4Se_8$. *J. Am. Chem. Soc.* **2005**, *127*, 8732−8740.
(19) Zhang, Q. R.; Rhodes, D.; Zeng, B.; Besara, T.; Siegrist, T.; Johannes, M. D.; Balicas, L. Anomalous metallic state and anisotropic multiband superconductivity in $Nb_3Pd_{0.7}Se_7$. *Phys. Rev. B: Condens. Matter Mater. Phys.* **2013**, *88*, 024508.
(20) Hu, J.; Gu, Y.; Le, C. Predicting diamond-like Co-based chalcogenides as unconventional high temperature superconductors. *Sci. Bull.* **2018**, *63*, 1338−1344.
(21) Chittari, B. L.; Lee, D.; Banerjee, N.; MacDonald, A. H.; Hwang, E.; Jung, J. Carrier- and strain-tunable intrinsic magnetism in two-dimensional MAX_3 transition metal chalcogenides. *Phys. Rev. B: Condens. Matter Mater. Phys.* **2020**, *101*, 085415.
(22) Yang, X.; Zhou, Y.; Wang, M.; Bai, H.; Chen, X.; An, C.; Zhou, Y.; Chen, Q.; Li, Y.; Wang, Z.; Chen, J.; Cao, C.; Li, Y.; Zhou, Y.; Yang, Z.; Xu, Z.-A. Pressure induced superconductivity bordering a charge-density-wave state in $NbTe_4$ with strong spin-orbit coupling. *Sci. Rep.* **2018**, *8*, 6298.
(23) Hull, G. W.; Hulliger, F. CuSe2, a Marcasite Type Superconductor. *Nature* **1968**, *220*, 257−258.
(24) Jiao, W.-H.; Tang, Z.-T.; Sun, Y.-L.; Liu, Y.; Tao, Q.; Feng, C.-M.; Zeng, Y.-W.; Xu, Z.-A.; Cao, G.-H. Superconductivity in a Layered $Ta_4Pd_3Te_{16}$ with $PdTe_2$ Chains. *J. Am. Chem. Soc.* **2014**, *136*, 1284−1287.
(25) Chen, L.-C.; Yu, H.; Pang, H.-J.; Jiang, B.-B.; Su, L.; Shi, X.; Chen, L.-D.; Chen, X.-J. Pressure-induced superconductivity in palladium sulfide. *J. Phys.: Condens. Matter* **2018**, *30*, 155703.
(26) Matsumoto, R.; Song, P.; Adachi, S.; Saito, Y.; Hara, H.; Yamashita, A.; Nakamura, K.; Yamamoto, S.; Tanaka, H.; Irifune, T.; Takeya, H.; Takano, Y. Pressure-induced superconductivity in tin sulfide. *Phys. Rev. B: Condens. Matter Mater. Phys.* **2019**, *99*, 184502.
(27) Dunn, K. J.; Bundy, F. P. Pressure-induced metallic and superconducting state of GaSe. *Appl. Phys. Lett.* **1980**, *36*, 709−710.
(28) Schwarz, U.; Olguin, D.; Cantarero, A.; Hanfland, M.; Syassen, K. Effect of pressure on the structural properties and electronic band structure of GaSe. *Phys. Status Solidi B* **2007**, *244*, 244−255.
(29) Ke, F.; Dong, H.; Chen, Y.; Zhang, J.; Liu, C.; Zhang, J.; Gan, Y.; Han, Y.; Chen, Z.; Gao, C.; Wen, J.; Yang, W.; Chen, X.-J.; Struzhkin, V. V.; Mao, H.-K.; Chen, B. Decompression-Driven Superconductivity Enhancement in In_2Se_3. *Adv. Mater.* **2017**, *29*, 1701983.
(30) Grochala, W.; Hoffmann, R.; Feng, J.; Ashcroft, N. W. The Chemical Imagination at Work in Very Tight Places. *Angew. Chem., Int. Ed.* **2007**, *46*, 3620−3642.
(31) Zhou, Y.; Zhang, B.; Chen, X.; Gu, C.; An, C.; Zhou, Y.; Cai, K.; Yuan, Y.; Chen, C.; Wu, H.; Zhang, R.; Park, C.; Xiong, Y.; Zhang, X.; Wang, K.; Yang, Z. Pressure-Induced Metallization and Robust Superconductivity in Pristine 1T-$SnSe_2$. *Adv. Electron. Mater.* **2018**, *4*, 1800155.
(32) Nilges, T.; Lange, S.; Bawohl, M.; Deckwart, J. M.; Janssen, M.; Wiemhöfer, H.-D.; Decourt, R.; Chevalier, B.; Vannahme, J.; Eckert, H.; Weihrich, R. Reversible switching between p- and n-type conduction in the semiconductor $Ag_{10}Te_4Br_3$. *Nat. Mater.* **2009**, *8*, 101.
(33) Hull, S.; Keen, D. A.; Hayes, W.; Gardner, N. J. G. Superionic behaviour in copper (I) iodide at elevated pressures and temperatures. *J. Phys.: Condens. Matter* **1998**, *10*, 10941.
(34) Lin, W.; Stoumpos, C. C.; Kontsevoi, O. Y.; Liu, Z.; He, Y.; Das, S.; Xu, Y.; McCall, K. M.; Wessels, B. W.; Kanatzidis, M. G. $Cu_2I_2Se_6$: A Metal-inorganic Framework Wide-Bandgap Semiconductor for Photon Detection at Room Temperature. *J. Am. Chem. Soc.* **2018**, *140*, 1894−1899.
(35) Cai, W.; Lin, W.; Li, L.-H.; Malliakas, C. D.; Zhang, R.; Groesbeck, M.; Bao, J.-K.; Zhang, D.; Sterer, E.; Kanatzidis, M. G.; Deemyad, S. Pressure-Induced Superconductivity and Flattened Se6 Rings in the Wide Band Gap Semiconductor $Cu_2I_2Se_6$. *J. Am. Chem. Soc.* **2019**, *141*, 15174−15182.
(36) Sarfati, J. D.; Burns, G. R. The pressure, temperature and excitation frequency dependent Raman spectra; and infrared spectra of $CuBrSe_3$ and $CuISe_3$. *Spectrochim. Acta* **1994**, *50*, 2125−2136.
(37) Klotz, S; Chervin, J-C; Munsch, P; Le Marchand, G Hydrostatic limits of 11 pressure transmitting media. *J. Phys. D: Appl. Phys.* **2009**, *42*, 075413.
(38) Chen, X.; Lu, P.; Wang, X.; Zhou, Y.; An, C.; Zhou, Y.; Xian, C.; Gao, H.; Guo, Z.; Park, C.; Hou, B.; Peng, K.; Zhou, X.; Sun, J.; Xiong, Y.; Yang, Z.; Xing, D.; Zhang, Y. Topological Dirac line nodes and superconductivity coexist in SnSe at high pressure. *Phys. Rev. B: Condens. Matter Mater. Phys.* **2017**, *96*, 165123.
(39) Emery, V. J.; Kivelson, S. A. Superconductivity in Bad Metals. *Phys. Rev. Lett.* **1995**, *74*, 3253−3256.
(40) Efros, A. L.; Shklovskii, B. I. Critical Behaviour of Conductivity and Dielectric Constant near the Metal-Non-Metal Transition Threshold. *Phys. Status Solidi B* **1976**, *76*, 475−485.
(41) Wilke, S. Bond percolation threshold in the simple cubic lattice. *Phys. Lett. A* **1983**, *96*, 344−346.
(42) Shklovskii, B. I.; Efros, A. L. *Electronic Properties of Doped Semiconductors*; Springer-Verlag: Berlin, 1984; pp 94−130.
(43) Sahimi, M. Finite-size scaling calculation of conductivity of three-dimensional conductor-superconductor networks at percolation threshold. *J. Phys. C: Solid State Phys.* **1984**, *17*, L355−L358.
(44) Clogston, A. M. Upper Limit for the Critical Field in Hard Superconductors. *Phys. Rev. Lett.* **1962**, *9*, 266−267.
(45) Dronskowski, R.; Bloechl, P. E. Crystal orbital Hamilton populations (COHP): energy-resolved visualization of chemical bonding in solids based on density-functional calculations. *J. Phys. Chem.* **1993**, *97*, 8617−8624.
(46) Allen, P. B.; Dynes, R. C. Transition temperature of strong-coupled superconductors reanalyzed. *Phys. Rev. B* **1975**, *12*, 905−922.
(47) Mao, H. K.; Bell, P. M.; Shaner, J. W.; Steinberg, D. J. Specific volume measurements of Cu, Mo, Pd, and Ag and calibration of the ruby R_1 fluorescence pressure gauge from 0.06 to 1 Mbar. *J. Appl. Phys.* **1978**, *49*, 3276−3283.
(48) Bruker. *APEX3*; Bruker AXS Inc.: Madison, WI, 2016.
(49) Sheldrick, G. A short history of SHELX. *Acta Crystallogr., Sect. A: Found. Crystallogr.* **2008**, *64*, 112−122.
(50) Dolomanov, O. V.; Bourhis, L. J.; Gildea, R. J.; Howard, J. A. K.; Puschmann, H. OLEX2: a complete structure solution, refinement and analysis program. *J. Appl. Crystallogr.* **2009**, *42*, 339−341.
(51) Prescher, C.; Prakapenka, V. B. DIOPTAS: a program for reduction of two-dimensional X-ray diffraction data and data exploration. *High Pressure Res.* **2015**, *35*, 223−230.
(52) Toby, B. EXPGUI, a graphical user interface for GSAS. *J. Appl. Crystallogr.* **2001**, *34*, 210−213.
(53) Savin, A. The electron localization function (ELF) and its relatives: interpretations and difficulties. *J. Mol. Struct.: THEOCHEM* **2005**, *727*, 127−131.
(54) Kresse, G.; Furthmüller, J. Efficient iterative schemes for ab initio total-energy calculations using a plane-wave basis set. *Phys. Rev. B: Condens. Matter Mater. Phys.* **1996**, *54*, 11169−11186.
(55) Kresse, G.; Joubert, D. From ultrasoft pseudopotentials to the projector augmented-wave method. *Phys. Rev. B: Condens. Matter Mater. Phys.* **1999**, *59*, 1758−1775.
(56) Perdew, J. P.; Burke, K.; Ernzerhof, M. Generalized Gradient Approximation Made Simple. *Phys. Rev. Lett.* **1996**, *77*, 3865−3868.
(57) Blöchl, P. E. Projector augmented-wave method. *Phys. Rev. B: Condens. Matter Mater. Phys.* **1994**, *50*, 17953−17979.
(58) Grimme, S.; Antony, J.; Ehrlich, S.; Krieg, H. A consistent and accurate ab initio parametrization of density functional dispersion correction (DFT-D) for the 94 elements H-Pu. *J. Chem. Phys.* **2010**, *132*, 154104.
(59) Monkhorst, H. J.; Pack, J. D. Special points for Brillouin-zone integrations. *Phys. Rev. B* **1976**, *13*, 5188−5192.
(60) Deringer, V. L.; Tchougréeff, A. L.; Dronskowski, R. Crystal Orbital Hamilton Population (COHP) Analysis As Projected from Plane-Wave Basis Sets. *J. Phys. Chem. A* **2011**, *115*, 5461−5466.

https://dx.doi.org/10.1021/acs.chemmater.0c02151
Chem. Mater. 2020, 32, 6237−6246

(61) Maintz, S.; Deringer, V. L.; Tchougréeff, A. L.; Dronskowski, R. LOBSTER: A tool to extract chemical bonding from plane-wave based DFT. *J. Comput. Chem.* **2016**, *37*, 1030−1035.
(62) Togo, A.; Oba, F.; Tanaka, I. First-principles calculations of the ferroelastic transition between rutile-type and $CaCl_2$-type SiO_2 at high pressures. *Phys. Rev. B: Condens. Matter Mater. Phys.* **2008**, *78*, 134106.
(63) Giannozzi, P.; Baroni, S.; Bonini, N.; Calandra, M.; Car, R.; Cavazzoni, C.; Ceresoli, D.; Chiarotti, G. L.; Cococcioni, M.; Dabo, I.; Dal Corso, A.; de Gironcoli, S.; Fabris, S.; Fratesi, G.; Gebauer, R.; Gerstmann, U.; Gougoussis, C.; Kokalj, A.; Lazzeri, M.; Martin-Samos, L.; Marzari, N.; Mauri, F.; Mazzarello, R.; Paolini, S.; Pasquarello, A.; Paulatto, L.; Sbraccia, C.; Scandolo, S.; Sclauzero, G.; Seitsonen, A. P.; Smogunov, A.; Umari, P.; Wentzcovitch, R. M. QUANTUM ESPRESSO: a modular and open-source software project for quantum simulations of materials. *J. Phys.: Condens. Matter* **2009**, *21*, 395502.
(64) Troullier, N.; Martins, J. L. Efficient pseudopotentials for plane-wave calculations. *Phys. Rev. B: Condens. Matter Mater. Phys.* **1991**, *43*, 1993−2006.

https://dx.doi.org/10.1021/acs.chemmater.0c02151
Chem. Mater. 2020, 32, 6237−6246